Ion shaping of single-layer Au nanoparticles in amorphous silicon dioxide, in silicon nitride, and at their interface

P. Mota-Santiago,[1] F. Kremer,[2] G. Rizza,[3] C. Dufour[4], V. Khomenkov[4,5], C. Notthoff,[1] A. Hadley[1], and P. Kluth[1]

[1]*Department of Electronic Materials Engineering, Research School of Physics, Australian National University, Canberra ACT 2601, Australia*
[2]*Centre for Advanced Microscopy, Australian National University, Canberra ACT 2601, Australia*
[3]*Laboratoire des Solides Irradiés, Ecole Polytechnique, UMR 7642 CEA, DSM, IRAMIS,
Centre National de la Recherche Scientifique, Palaiseau Cedex, France*
[4]*CIMAP/ENSICAEN, 6 Boulevard du Maréchal Juin, Caen Cedex, France*
[5]*Institute for Nuclear Research, 47 Nauky Avenue, Kyiv, Ukraine*

We present the shape transformation of a single layer of Au nanoparticles (NPs) when embedded in, and at the interface of, amorphous SiN_x and SiO_x (a-SiN_x and a-SiO_x) thin films upon irradiation with 185-MeV Au ions to fluences ranging from 0.3 to 30×10^{13} cm^{-2}. Transmission electron microscopy (TEM) and high angular annular dark field microscopy were used to study the ion-shaping process. The former allows us to follow the overall change in geometry, size, and structure, while the latter reveals information about the relative position with respect to the interface. For Au NPs embedded in a single material, a lower elongation rate for a-SiN_x was found in comparison to a-SiO_x. When at the interface of the two materials, TEM reveals a preferential elongation towards a-SiO_x. The latter demonstrates the use of a-SiN_x for confining the ion-shaping process within an intermediate a-SiO_x layer. The simulation of the temperature evolution during a single-ion impact was used to understand the difference in elongation rates between a-SiN_x and a-SiO_x, as well as the asymmetric behavior when located at the interface using the three-dimensional inelastic thermal spike model with bulk thermophysical properties. The calculations show good agreement with the experimental observations and reveal a correlation between the thermal profile and the resulting NP geometry.

I. INTRODUCTION

Much research on metallic nanostructures has been carried out in the past decades due to the advent of many promising applications using the coupling between photons and the conduction electrons at metal interfaces in the near ultraviolet, visible, and near-infrared range, a field known as plasmonics [1,2]. Plasmonic devices have attracted significant interest because of the possibility of subwavelength confinement of light and the local intensity enhancement of electromagnetic fields. A special focus has been set on the design of metal-dielectric nanocomposites because their interesting optical response can be tuned by engineering the volume, geometry, orientation, metal species, and dielectric function of the surrounding medium [3]. Dielectric materials containing embedded metallic nanostructures with controlled anisotropy are of great interest for a broad range of applications. They have been used to manipulate light-matter interactions arising from the coupling of oscillating external electromagnetic fields with the conduction electrons in metallic nanoparticles (MNPs), known as localized surface-plasmon resonances. By controlling the NP anisotropy, it is possible to modify the linear and nonlinear optical response of the host material as their response is dependent on size and geometry of the NPs. MNPs of different shapes have found applications as nanoantennas, to store energy in the free-electron movement [4,5] and manipulate light at the nanoscale [6–9]. For example, anisotropic Au NPs embedded in α-Al_2O_3 present interesting nonlinear optical properties. When the incident light is polarized parallel to the major axis of the Au NPs, the resulting signal exhibits a large nonlinear reflectivity and small nonlinear absorbance, making it a good candidate for all-optical switching technologies [10].

While many fabrication methods for metal-dielectric nanocomposites are available, among the most widespread are chemical synthesis of metal colloids and core-shell particles, self-organization, electron-beam lithography, and nanoimprinting [11]. Ion irradiation of metallic NPs with swift heavy ions has demonstrated the possibility to transform spherical NPs into well-aligned and high-aspect-ratio nanorods while embedded in a dielectric medium, a process often termed "ion shaping" [12,13].

The ion-shaping process of metal NPs has been studied predominantly with a-SiO_2 as the host matrix [10] with various metallic species such as Au [14–19], Ag [20,21], Co [12], Ni [22,23], Zn [6,24,25], V [26], and metal alloys [27,28]. In the ion-shaping process, the composite material is irradiated with energetic ions, which penetrate the solid and interact predominantly via inelastic interactions with the material's electrons. A number of mechanisms have been proposed to be operational during the ion-shaping process that remain under study and debate. One model proposes the shape transformation of a transiently molten MNP due to the in-plane stress resulting from the ion hammering effect [29]. Another model explains the process as the result of the NP thermal expansion

and flow into the underdense core region of the formed track [30]. While both models discuss two different pathways of deformation, both assume a transient molten state produced by the thermal spike effect [31].

When a swift heavy ion penetrates a solid, it will interact predominantly with valence and core electrons, leading to the charge redistribution resulting from the production of energetic electrons, so-called δ electrons, as a result of the deposition of large amounts of energy into the electronic system. The overall movement of the energetic electrons leads to a charge separation perpendicular to the ion trajectory, producing secondary ionization, positive holes, and the corresponding formation of a transverse electric field. Auger transitions and secondary ionization occur within a few femtoseconds and a trace of energetic electrons and holes is formed within the δ-electron range, up to a few hundred nanometers away from the ion trajectory [32,33]. This leads to a radially polarized region composed of a positive inner region populated by valence-band holes and energetic electrons in the outer region. Yet, the transient electric field vanishes on a femtosecond scale, earlier than atomic motion can occur in most materials, due to depolarization [34]. Depolarization leads to the recovery of spatial net charge neutralization, although the electrons remain excited [32]. This can be considered a preamble for the rapid increase in the lattice temperature, known as the thermal spike that will cause the main structural modifications in the material [32,35]. However, this initial stage has not been discussed with regards to its influence on the ion-shaping process.

The highly excited electrons transfer part of their energy to the atomic lattice, leading to local heating (thermal spike) that can induce structural modifications in the matrix known as ion tracks [36]. Recently, the morphology of such ion tracks has been determined for a-SiO$_2$ and a-Si$_3$N$_4$ consisting of a cylindrical geometry formed by an underdense core surrounded by an overdense shell relative to the bulk density [36,37]. In the case of the embedded metallic NPs, it is known that the energy transfer from the electronic system towards the atomic lattice is less efficient than in the matrix. The structural modification was then proposed to be driven by the difference in the energy-transfer efficiency at the boundary of the NP and the matrix, a process known as the outer boundary heating process [38]. In this model, the modification of the metallic NPs is dependent on their degree of melting, which depends on the nanoparticle volume and sets an upper size limit for the elongation to occur. Later, molecular dynamics (MD) simulations of the ion-shaping dynamics for Au NPs embedded in a-SiO$_2$ showed that the process is confined to the core region of the ion track formed in the matrix surrounding the NP [30]. According to the MD simulation results, this occurs as the track formation process and the melting of the Au NP coexist for up to 20 ps, time enough for the NP to expand towards the track region. Unfortunately, the process was only studied for one experimental condition. An attempt to bridge this limitation was carried out by a new theoretical study, proposed to follow the complete shaping process for a wider range of Au NP sizes using a phenomenological simulation code based on the expansion/recrystallization mechanism observed by MD simulations [39]. As a result, it was concluded that the NP cannot completely expand into the matrix during the

ion-shaping process and should be limited by the time of the track formation and the expansion process, suggesting that the matrix strongly resists the expansion of the Au NP afterwards. Yet, the role of the morphology and lifetime of the ion track formation process is still unclear.

As the plasmonic response of these systems is dependent on the dielectric function of the host matrix [3], it is highly desired to extend the approach developed for a-SiO$_2$ to other dielectric materials. The present paper reports on the ion-shaping process of Au nanoparticles embedded in a-SiN$_{1.06}$ and a-SiO$_{1.9}$ deposited by plasma enhanced chemical vapor deposition (PECVD), and at the interface of the two materials. The experiments aimed to provide a comparison regarding the ion shaping of Au NPs in a different matrix (a-Si$_3$N$_4$) with respect to a-SiO$_2$, and at the interface of the two dielectrics to highlight the role of the matrix thermophysical properties on the ion-shaping process. The results have been divided into four subsections. Section III A reports on the ion shaping of Au NPs while embedded in a-SiN$_{1.06}$ or a-SiO$_{1.9}$, Sec. III B reports on the ion shaping at the interface of the two dielectric materials, Sec. III C assesses the effect of the thermophysical properties on the ion-shaping process using the three-dimensional thermal spike model, and Sec. III D presents the use of a-SiN$_{1.06}$ as a diffusion barrier capable of confining the ion shaping to a sandwiched a-SiO$_{1.9}$ thin layer. The NP shape and size evolution was characterized by TEM and high angular annular dark field prior to and after irradiation to 0.3×10^{13}, 3×10^{13}, and 10×10^{13} ions cm^{-2}. The experimental observations are accompanied by three-dimensional simulations of a single-ion impact using the three-dimensional inelastic thermal spike (i-TS) model. Differences in the thermal properties, as well as the strength of the electron-phonon coupling between the two materials, are proposed as potential driving forces for the different shaping rates observed.

II. EXPERIMENTAL

A. Synthesis of single-layer Au NPs in amorphous silicon nitride, in silicon dioxide, and at their interface

The synthesis of single-layer Au NPs proceeds by depositing an initial a-SiN$_{1.06}$ or a-SiO$_{1.9}$ thin layer with a thickness up to 500 nm on top of a c-Si (100) wafer by PECVD. This is followed by the deposition of a 5-nm Au layer by thermal evaporation. The thin metallic layer is then covered by a second layer of a-SiO$_{1.9}$ or a-SiN$_{1.06}$ using PECVD with a thickness of up to 500 nm. The process is summarized in Fig. 1. The characterization of the physical properties and deposition conditions of the two dielectric layers has been reported elsewhere [36]. After deposition of the top layer, the samples are annealed in a rapid thermal annealing (RTA) process (using an AET RX system) for 2 min at 1000 °C in a N$_2$ atmosphere. While the thin Au layer in Figs. 1(c) and 1(d) appears to be continuous before annealing, the formation of islands or small clusters due to the temperatures involved during the deposition of the top layer cannot be ruled out. In Fig. 1(e), a plan view image by scanning electron microscopy shows formed Au NPs after thinning down the top layer by inductively coupled plasma etching.
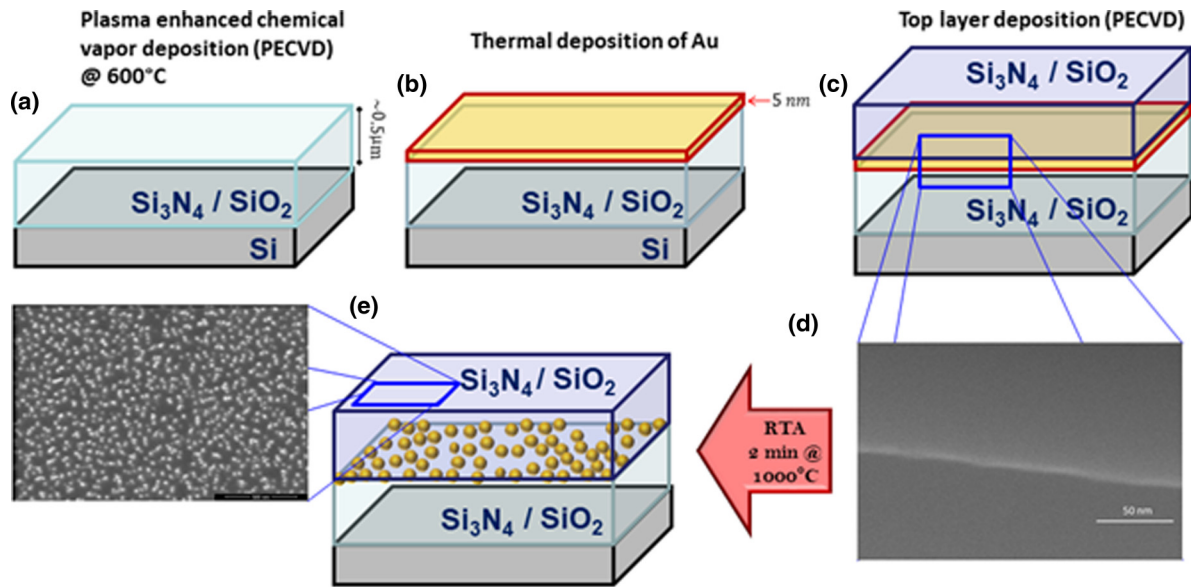
FIG. 1. Schematic of the sequential depositions using PECVD a-SiN$_{1.06}$ and a-SiO$_{1.9}$ and thermal deposition of a thin Au layer. After thermal annealing, a single layer of Au NPs is formed. Cross-sectional and plan view scanning electron microscopy micrographs have been added to exemplify the continuous Au layer formed after deposition of the top layer and the NP density after RTA, respectively.

To demonstrate the use of a-SiN$_{1.06}$ as a layer to confine the ion-shaping process, the design and fabrication of the system are depicted in Fig. 2 and consist of two a-SiN$_{1.06}$ layers (top and bottom) with thickness of 160.0 ± 0.2 nm and an intermediate a-SiO$_{1.9}$ layer of 140.2 ± 0.1-nm thickness deposited by PECVD. The synthesis of a single Au NP layer was carried out under the same conditions as for the previous samples. For this purpose, the 5-nm-thick Au layer was deposited between the bottom a-SiN$_{1.06}$ and the intermediate a-SiO$_{1.9}$ layers.

As shown in the schematics in Fig. 3, five combinations of layers were deposited by PECVD: a-SiN$_{1.06}$/a-SiN$_{1.06}$, a-SiO$_{1.9}$/a-SiO$_{1.9}$, a-SiO$_{1.9}$/a-SiN$_{1.06}$, a-SiN$_{1.06}$/a-SiO$_{1.9}$, and a-SiN$_{1.06}$/a-SiO$_{1.9}$/a-SiN$_{1.06}$. Upon annealing, the thin Au layer transforms into Au droplets by spinodal dewetting, becoming polycrystalline after resolidification (Fig. 3) [40]. The Au NPs exhibit a spheroidal geometry, which can be described by two axes: the parallel (width) and the perpendicular (length) to the surface. Cross-sectional TEM was carried out to characterize the parallel and perpendicular dimensions of Au NPs formed in the four significant deposition configurations. The values are summarized in Table I after consideration of at least 150 NPs in each case.

After annealing, only small differences between the parallel and perpendicular axis of the formed Au NPs are observed for the four fundamental configurations, exhibiting a mean size of nearly 20 and 16 nm for the parallel and perpendicular axis, respectively, while differences between the different configurations are within 10%. Furthermore, the size distribution of Au NPs did not exhibit a strong dependence on the surrounding medium and, thus, the elongation process can be directly compared between all configurations. When the Au NPs are located at the interface of a-SiN$_{1.06}$ and a-SiO$_{1.9}$, TEM micrographs show that the NPs are not located right at the interface of the two materials but exhibit a small shift into the top layer, creating an asymmetrical position of the NPs at the interface. As seen in Figs. 3(c) and 3(d), the layer deposited on top is the predominant embedding medium, with an average shift of the NPs of 5 ± 1.5 nm upwards. A possible explanation for the asymmetrical configuration could be the occurrence of dewetting during the deposition of the top layer, which occurs at 600 °C for between 5 and 10 min, before the RTA step. The effect of the asymmetry on the ion-shaping process will be further discussed in the last section of this paper as it plays an important role in the final geometry of the irradiated Au NPs.
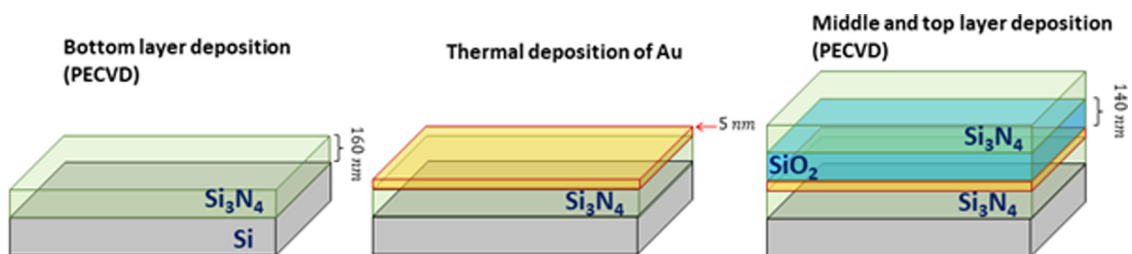
FIG. 2. Fabrication process of the multilayer system using two a-SiN$_{1.06}$ thin layers as a diffusion barrier.
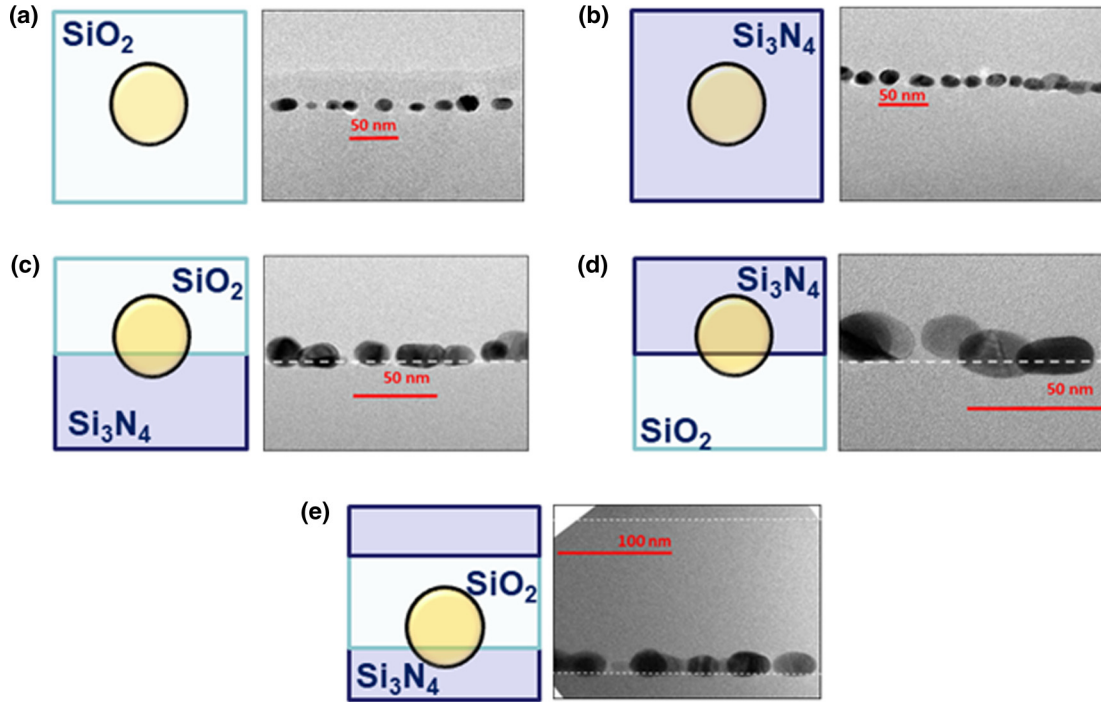
FIG. 3. Schematic and TEM micrographs of the cross-sectional cut of Au NPs formed in a-SiO$_{1.9}$, in a-SiN$_{1.06}$, and at the interface of the two materials. Dashed lines were added to highlight the relative position of the interface.

B. Three-dimensional inelastic thermal spike calculations

The temperature evolution of a single Au NP embedded in a-SiO$_{1.9}$, a-SiN$_{1.06}$ and at the interface of the two materials was carried out using the three-dimensional version of the inelastic thermal spike model (3D-iTS) developed by Dufour *et al.* [38], to provide further insight into the differences of the elongation process in the different dielectric media. It is considered a two- and three-component system, for the single and interface case, respectively, within a three-dimensional cell in Cartesian coordinates. For the case of one Au NP located at the interface, it is possible to offset the position of the Au NP to emulate the initial conditions, as observed in Fig. 3.

The energy-loss rates were estimated by the SRIM code [41] for a-SiO$_{1.9}$, a-SiN$_{1.06}$, and Au at the surface, to match the experimental conditions. At a total layer thickness of ≈ 1 μm the electronic energy-loss rate does not change significantly and can be estimated by the surface values using the SRIM code [41], to 20.9, 50.0, and 16.3 keV/nm for a-SiN$_{1.06}$, Au and a-SiO$_{1.9}$, respectively.

The calculations were performed considering a spherical Au NP with a diameter of 16 nm centered in a cubic cell of $60 \times 60 \times 60$ nm^3. The surrounding medium was approximated by the known bulk properties of a-SiO$_2$, and a-Si$_3$N$_4$

as expressed in Ref. [36] under the considerations outlined by [38]. In the case of Au, bulk values are considered, as in Ref. [38], in particular as thermophysical corrections for the dimensions of the NPs can be neglected for the size studied [23]. The electron-phonon coupling values for the two dielectric materials were estimated based on the relation known between the optical band gap and the electron mean free path (λ). The former was measured by spectral reflectometry to be 4.9 $\pm$ 0.3 eV for a-SiN$_{1.06}$ and 9.1 $\pm$ 0.2 eV for a-SiO$_{1.9}$ [36,42]. Because of the difference in the optical band gap, the corresponding electron-phonon coupling is relatively low in silicon nitride $g_{\mathrm{Si_3N_4}} = 0.52 \times 10^{13}$ W/cm^3 K^{-1} in comparison with the case of silicon dioxide ($g_{\mathrm{SiO_2}} = 1.25 \times 10^{13}$ W/cm^3 K^{-1}), leading to a lower energy transfer from the electronic subsystem into the lattice.

III. RESULTS AND DISCUSSION

A. Ion shaping of Au NPs in amorphous silicon dioxide and silicon nitride

Cross-section TEM micrographs of Au NPs embedded in a-SiO$_{1.9}$ and a-SiN$_{1.06}$ before and after irradiation with 185-MeV Au ions to different fluences are shown in Figs. 4(a) and

TABLE I. Parallel and perpendicular axis dimensions of Au NPs formed for the configurations presented in Figs. 3(a)–3(d). The uncertainties correspond to the standard deviation of a normal distribution.

a-SiN$_{1.06}$/a-SiN$_{1.6}$		a-SiO$_{1.9}$/a-SiO$_{1.9}$		a-SiO$_{1.9}$/a-SiN$_{1.06}$		a-SiN$_{1.06}$/a-SiO$_{1.9}$	
L (nm)	W (nm)	L (nm)	W (nm)	L (nm)	W (nm)	L (nm)	W (nm)
20.2 $\pm$ 3.9	16.0 $\pm$ 2.5	19.9 $\pm$ 7.1	16.0 $\pm$ 4.5	18.8 $\pm$ 4.1	15.9 $\pm$ 2.9	19.0 $\pm$ 4.3	17.0 $\pm$ 3.6
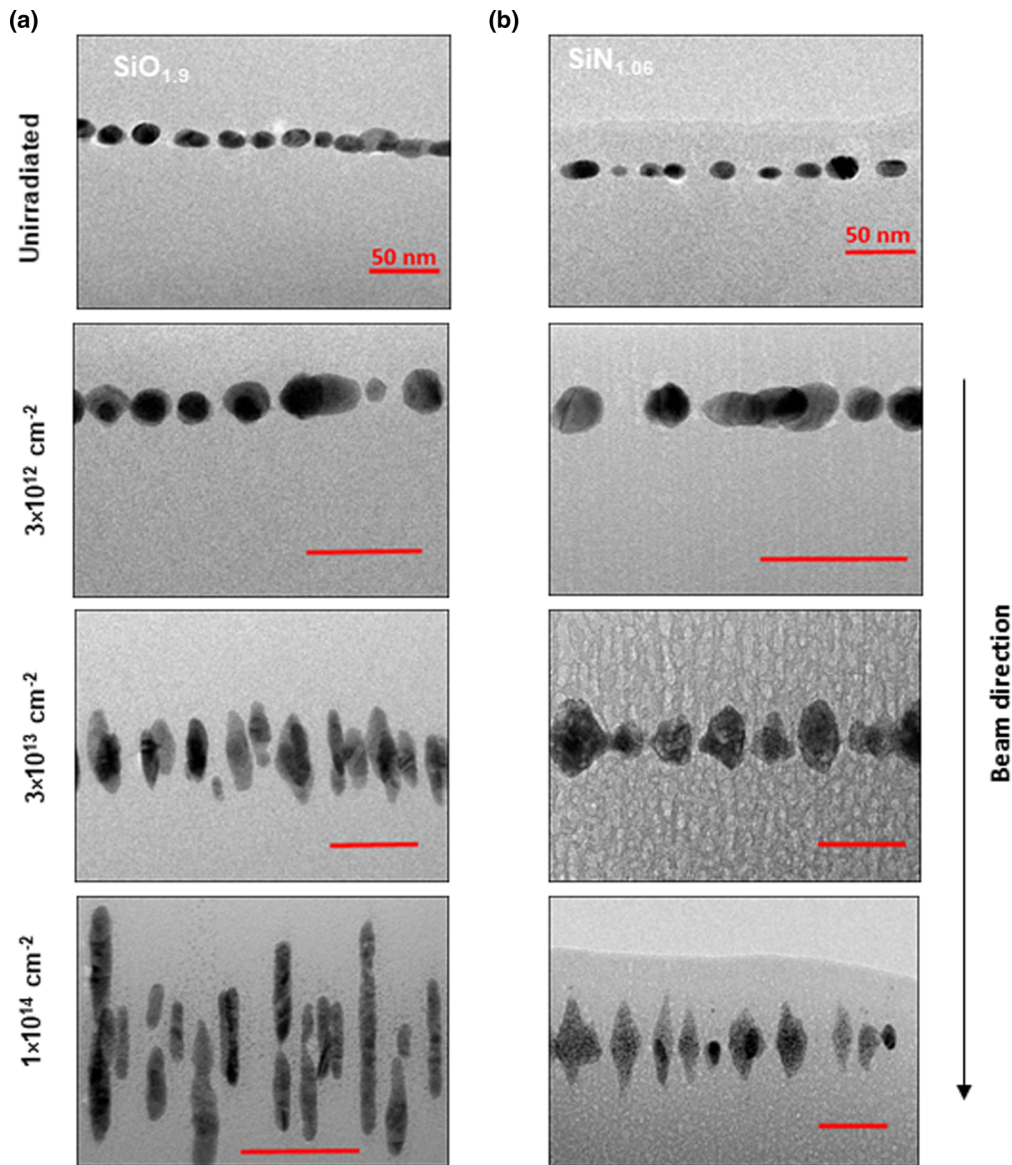
FIG. 4. Cross-section TEM (XTEM) images of Au NPs prior to and after irradiation with 185-MeV Au ions with different fluences (as indicated on the panel) for a-SiO$_{1.9}$ (a) and a-SiN$_{1.06}$ (b). An arrow indicating the beam direction has been added for clarity.

4(b), respectively. Prior to irradiation, the Au NPs exhibit a spheroidal geometry.

In the case of a-SiO$_{1.9}$, the transformation from spheroids to high aspect-ratio nanorods with increasing fluence is similar to the elongation observed previously in thermally grown a-SiO$_2$ [16,18,23]. At lower fluences (3×10^{12} cm^{-2}) the NPs become spherical prior to exhibiting clear prolate shapes at higher fluences. After irradiation to a fluence of 3×10^{13} cm^{-2}, the NPs present aspect ratios between 2:1 and 6:1, with an average length and width of 40.6 ± 6.1 and 13.7 ± 3.3 nm, respectively. The uncertainties correspond to the standard deviation of a normal distribution. At the highest fluence (1×10^{14} cm^{-2}) the prolate NPs are transformed into long nanorods, with mean values of 64.0 ± 18.7 and 7.5 ± 1.6 nm for the length and width and aspect ratios between 4:1 and 16:1, similar to the trend observed previously for elongated Au NPs embedded in thermally grown a-SiO$_2$ [16,23]. In the vicinity of the anisotropic NPs, small Au

NPs with diameters below 2 nm are observed. The so-called nanosatellites increase in density with increasing fluence [23].

Figure 4(b) shows the shape transformation of Au NPs embedded in a-SiN$_{1.06}$. Upon ion irradiation, the Au nanoparticles first exhibit a transition from spheroidal shapes towards a spherical geometry at fluences around 3×10^{12} cm^{-2}, similar to the previous case. This is followed by the formation of prolate NPs for 3×10^{13} cm^{-2} with aspect ratios between 1:1 and 2:1, and mean length and width of 32.6 ± 5.4 and 26.6 ± 5.6 nm, respectively. At the highest fluence, the presence of elongated Au NPs with an aspect ratio between 2:1 and 6:1 can be observed with mean values of 62 ± 14.4 and 17.9 ± 2.9 nm for length and width, respectively. However, the shape resembles a more rhombic-like geometry instead of a nanorod. In addition, in the fluence series presented in Fig. 4(b) it is possible to observe the formation of discontinuous defective voidlike regions accompanying the elongation process. For a fluence of 3×10^{12} cm^{-2} the voids exhibit a
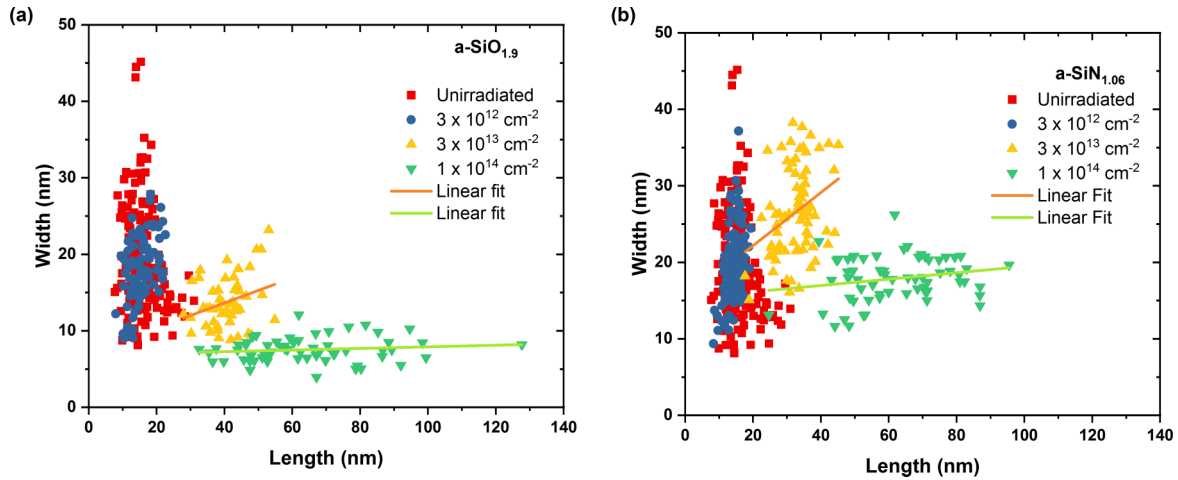
FIG. 5. Plot of the width vs length of the NPs determined by XTEM, for the fluences considered for a-SiO$_{1.9}$ (a) and a-SiN$_{1.06}$ (b).

narrow width and are aligned parallel to the beam direction. With increasing fluences, the width of the defective regions increases, while retaining their directionality.

The relationship between width and length of the Au NPs before and after ion irradiation for different fluences is plotted in Figs. 5(a) and 5(b) for a-SiO$_{1.9}$ and a-SiN$_{1.06}$, respectively. The continuous solid lines correspond to the mean width as a function of the length of the NP and were added to show the deformation process and the occurrence of the saturation of the width with increasing fluence. When Au NPs are embedded in a-SiO$_{1.9}$, after irradiation with 3×10^{13} cm^{-2}, the NPs exhibited an aspect ratio between 3:1 and 6:1 with a mean value of 4:1. For a-SiN$_{1.06}$ at the same irradiation fluence the aspect ratio of the Au NPs was determined by comparing the length of the minor (width) and major (length) axes, where lower values, between 1:1 and 2:1 with a mean aspect ratio of 1.4:1, were observed. At the maximum fluence, the aspect ratios of Au NPs in a-SiO$_{1.9}$ showed values between 4:1 and 16:1, and between 2:1 and 4.5:1 in the case of a-SiN$_{1.06}$. At this stage in a-SiO$_{1.9}$ NPs have an almost constant width of nearly 8.2 ± 0.5 nm, which is lower than the value of 10 nm previously reported for thermal SiO$_2$ [16] but similar to the saturation width observed in Au-Ag alloys [27] under similar irradiation conditions. Because the a-SiO$_{1.9}$ layers were deposited by PECVD, they commonly exhibit residual H content as well as stoichiometric and density differences compared to thermal SiO$_2$. Such differences might be correlated to the difference in the saturation width observed. In the case of a-SiN$_{1.06}$, after irradiation with 1×10^{14} cm^{-2} the mean relationship between width and length exhibits an almost zero slope at widths of about twice that of the saturation width in a-SiO$_{1.9}$.

B. Ion shaping of Au NPs at the interface of amorphous silicon nitride and silicon dioxide

Figure 6 shows the cross-section TEM images of Au NPs at the interface of a-SiO$_{1.9}$ and a-SiN$_{1.06}$ layers on top and bottom [Fig. 6(a)] and vice versa [Fig. 6(b)] prior to and after irradiation with 185 MeV Au ions at different fluences. The dashed lines were added to show the position of the interface

with respect to the Au NP single layer. Because the total layer thickness corresponds to ≈ 1 μm, similar to the previous subsection, the electronic energy-loss rate is considered constant along the ion trajectory with the values corresponding to those at the surface.

In the micrographs, the asymmetric relative position of the NP plane with respect to the interface is evident. It is observed that the top layer forms the main medium surrounding the Au NPs, covering approximately 80% of the NP surface. Such asymmetry is of great relevance, as briefly described in the introductory section, because the surrounding medium plays a key role in the ion-shaping process.

Figure 6(a) shows the shape transformation with a-SiN$_{1.06}$ as the bottom layer and a-SiO$_{1.9}$ as the top layer. At a fluence of 3×10^{12} cm^{-2}, we observe that Au NPs become spherical while it appears that the contact area with the bottom layer is reduced. Also, no observable irradiation damage is apparent in the a-SiO$_{1.9}$ region, while the a-SiN$_{1.06}$ layer shows narrow damage regions, similar to those described in the previous subsection. When the fluence increases to 3×10^{13} cm^{-2}, the transformation of the NPs into nanorods with an aspect ratio between 2:1 and 4:1 is observed where elongation mainly proceeds towards the a-SiO$_{1.9}$ layer while exhibiting a flat base at the interface, with very limited diffusion towards the a-SiN$_{1.06}$ layer (within 3–5 nm). Radiation damage formed in the a-SiN$_{1.06}$ layer is also evident, as well as the presence of very thin and long structures along the beam direction in the a-SiO$_{1.9}$ layer, which were not observed in the case of ion irradiated Au NPs embedded in only a-SiO$_{1.9}$. The observed nanorods exhibit a high aspect ratio with a mean length and width of 42.2 ± 18.1 and 11.2 ± 5.2 nm, respectively. When the highest fluence is reached (1×10^{14} cm^{-2}), we observe the transformation of the Au nanoparticles into high-aspect-ratio nanorods, comparable to the previous case of a-SiO$_{1.9}$ with a mean length and width of 77.1 ± 24.8 and 8.6 ± 2.1 nm, respectively, with some diffusion into the a-SiN$_{1.06}$ layer that shows very irregular shapes. The elongation process is also accompanied by the formation of porosity or voids inside the anisotropic Au NPs, with the majority observed in the NP region close to the a-SiN$_{1.06}$ interface.
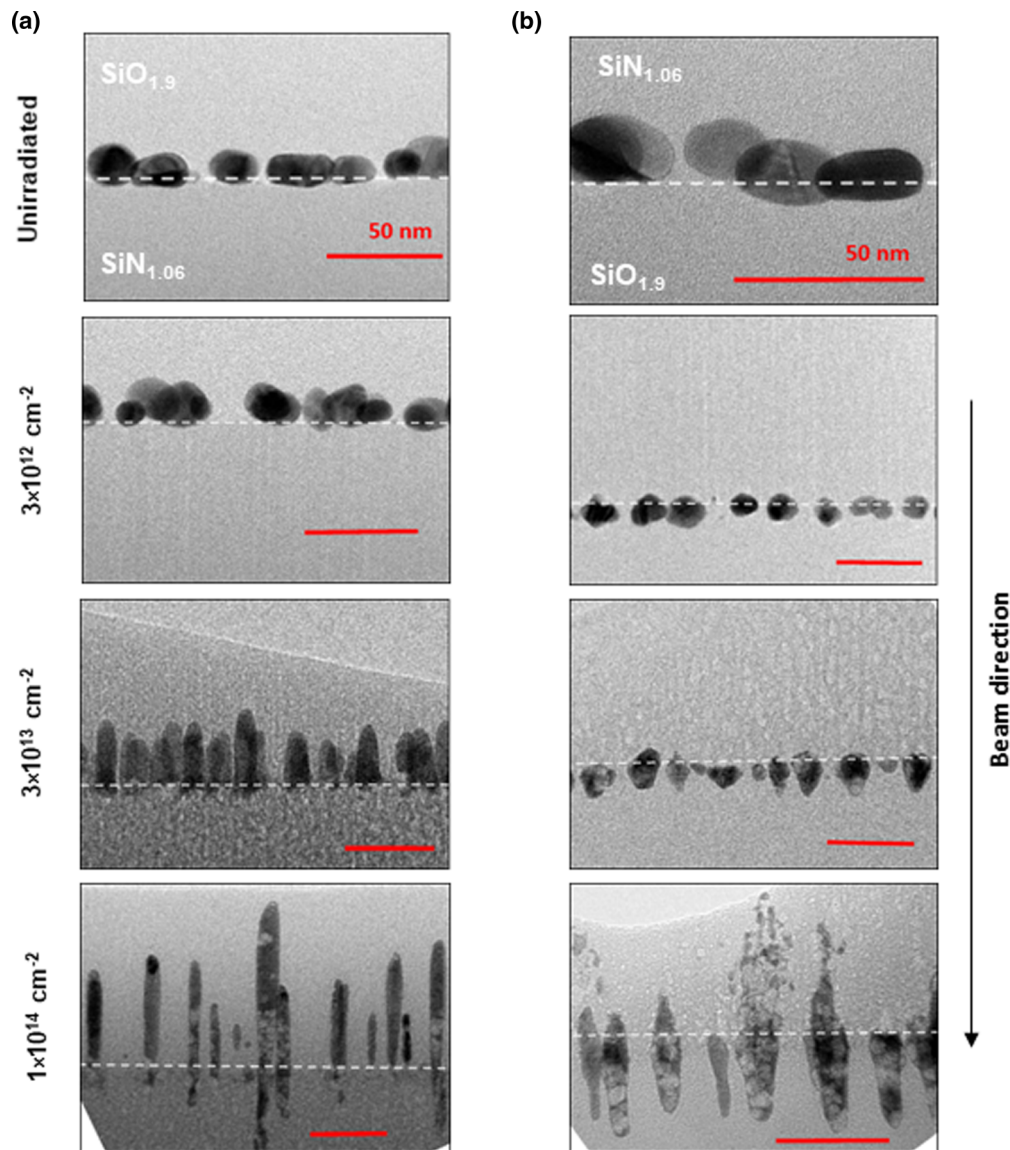
FIG. 6. Cross-section TEM (XTEM) images of Au NPs prior to and after irradiation with 185 MeV Au ions with different fluences (as indicated on the panel) located at the interface of a-$SiO_{1.9}$ and a-$SiN_{1.06}$, while being embedded predominantly in a-$SiO_{1.9}$ (a) or a-$SiN_{1.06}$ (b). An arrow indicating the beam direction has been added for clarity.

In the other configuration [Fig. 6(b)], the corresponding cross-section TEM images of Au NPs at the interface of a-$SiO_{1.9}$ and a-$SiN_{1.06}$ (bottom/top) layers prior to and after ion irradiation also exhibit a clear shape transformation with fluence. After irradiation to a fluence of 3×10^{12} cm^{-2}, we observe the transformation from spheroids into spheres. This is accompanied by a clear shift into the a-$SiO_{1.9}$ layer. When the fluence increases to 3×10^{13} cm^{-2}, the Au NPs are almost completely embedded in the a-$SiO_{1.9}$ layer. They show a transformation towards a prolate geometry with a mean length and width of 22.7 ± 4.4 and 18.9 ± 3.3 nm, respectively, while they are aligned with the beam direction and exhibit rough and sharp edges and nanoporous appearance. When reaching the maximum irradiation fluence of 1×10^{14} cm^{-2}, highly nanoporous nanorods with a mean aspect ratio around 5:1 and mean length and width of 60.6 ± 10.7 and 12.6 ± 2.0 nm, respectively, can be observed. Most of the NPs exhibit a flat

and broad end at the interface with a-$SiN_{1.06}$, yet irregular elongation towards the top layer was observed for some cases. In those cases, the ion-induced damage in the a-$SiN_{1.06}$ layer may facilitate the Au diffusion towards this region, noting that the elongation into this layer does not resemble the geometry observed in elongated NPs in a-$SiN_{1.06}$. For example, in Fig. 6(b) fragmented and discontinuous Au structures in a-$SiN_{1.06}$ with irregular shapes can be observed that resemble the ion induced damage structure in the a-$SiN_{1.06}$ region while this is not observed in the a-$SiO_{1.9}$ layer.

Figures 7(a) and 7(b) show the correlation between width and length of the Au NPs measured by TEM for the two multilayered systems, similar to the previous case. Due to the presence of irregular NP shapes, the width of each NP was measured at a distance of ≈ 5 nm from the interface (dashed lines) into the a-$SiO_{1.9}$ layer. The NP length was determined considering a straight line connecting both ends of the NP

(a)

(b)
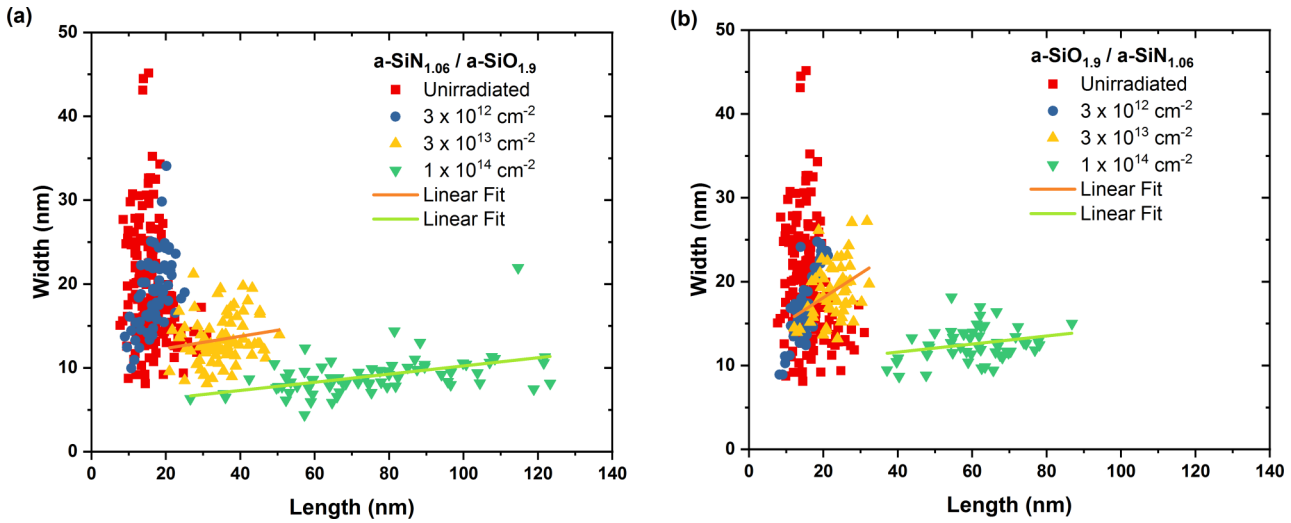
FIG. 7. Plot of the width vs length of the NPs determined by XTEM, for the fluences considered when a-SiO$_{1.9}$ (a) and a-SiN$_{1.06}$ (b) is the main surrounding matrix.

unless one end is not well defined, as for the NP at the center of the TEM image in Fig. 6(b) for the highest fluence. In this case the length was taken as the distance between the interface and the end of the NP in the a-SiO$_{1.9}$ layer. The solid lines represent the correlation trends for the fluences where clear elongation was observed. When a-SiO$_{1.9}$ is the main surrounding medium [Fig. 7(a)], the Au NPs present a spherical geometry after irradiation to 3×10^{12} cm^{-2} where an aspect ratio of nearly 1:1 was determined. After irradiation to a fluence of 3×10^{13} cm^{-2}, a reduction in the width is observed accompanied by an increase in the length of the NPs, exhibiting an aspect ratio between 2:1 and 3.5:1, below the values observed for Au NPs in a-SiO$_{1.9}$. For the highest fluence, the Au NPs become nanorods with aspect ratios between 4:1 and 14:1, similar to those of Au NPs in a-SiO$_{1.9}$, but clearly the slope differs from that in Fig. 5(a). Nevertheless, the values of the widths measured lie around 10 nm and below, suggesting a similar saturation of the width value to that of a-SiO$_{1.9}$. The difference in the slope might be a consequence of the NP elongation occurring in only one direction. In the other case, when a-SiN$_{1.06}$ is the main embedding medium [Fig. 7(b)], nearly spherical NPs are observed after irradiation to 3×10^{12} cm^{-2}, similar to the previous case; however, with increasing fluence (3×10^{13} cm^{-2}) Au NPs present an aspect ratio between 1:1 and 1.5:1. At the highest fluence, the NPs show a clear increase in the aspect-ratio values between 4:1 and 8:1, lower than any of the previously presented cases; nevertheless, the trend exhibits a similar slope as in Fig. 7(a) but with larger width values ($\approx$12 nm). Such behavior agrees well with the necessity of higher fluences to reach the saturation of the width due to the Au NP shift into the a-SiO$_{1.9}$ layer.

In Fig. 8 the mean aspect ratio of the elongated Au NPs is plotted as a function of the ion fluence for each studied system. For a fluence up to 1×10^{14} cm^{-2}, in a first approximation each system appears to follow a linear trend from which the mean elongation rate, defined as aspect ratio vs fluence, can be determined. For the current experimental conditions the determined rates correspond to 7.85 ± 0.09

and $2.85 \pm 0.20\ 1 \times 10^{-14}$ (ions/cm^{-2})$^{-1}$ when the embedded medium is solely a-SiO$_{1.9}$ or a-SiN$_{1.06}$, respectively, and 7.71 ± 0.36 and $4.04 \pm 0.44\ 1 \times 10^{-14}$ (ions/cm^{-2})$^{-1}$ when a-SiO$_{1.9}$ or a-SiN$_{1.06}$ is the principal embedding medium. The inset in Fig. 8 shows the comparison between each elongation rate towards a-SiO$_{1.9}$. It is clearly apparent that the process is only about half as efficient when embedded solely or mainly in a-SiN$_{1.06}$ compared to a-SiO$_{1.9}$, besides the electronic stopping power being 30% higher in a-SiN$_{1.06}$. This is potentially
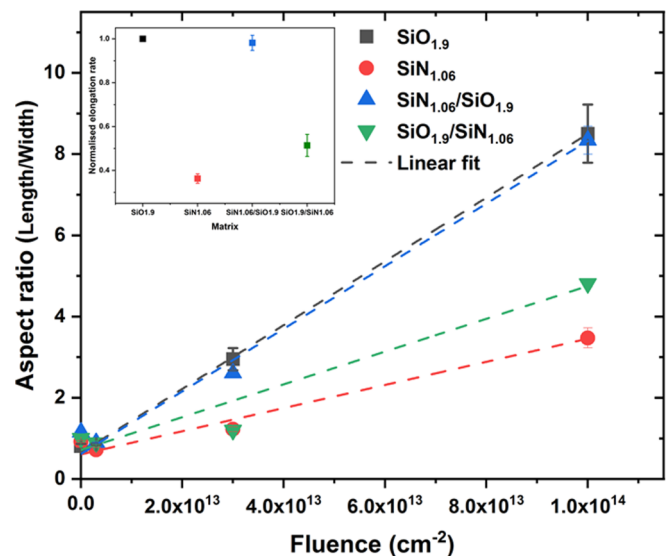
FIG. 8. Plot of the mean aspect ratio (length/width) as a function of fluence for the Au NPs embedded in the multilayer configurations under investigation: a-SiO$_{1.9}$ (black), a-SiN$_{1.06}$ (red), SiN$_{1.06}$/SiO$_{1.9}$ (blue), and SiO$_{1.9}$/SiN$_{1.06}$ (green). The dashed lines correspond to a linear fit for each system. The inset shows the elongation rate (slope) determined from the linear fit normalized with respect to a-SiO$_{1.9}$ as the only surrounding medium.

the result of the complex interrelation between thermal conductivity, electron-phonon coupling, and mean melting point, among others.

For both configurations, the formation of well-aligned voids in both layers (a-SiO$_{1.9}$ and a-SiN$_{1.06}$) can be observed, while such features were absent in Fig. 4(a). This indicates that the defects/voids originate in the a-SiN$_{1.06}$ layer and are able to migrate towards the a-SiO$_{1.9}$ layer, possibly by diffusion through the underdense core of the ion track in a-SiO$_{1.9}$. This suggests that the timescale at which the temperature inside the ion track remains above and near the melting point of a-SiO$_2$ is sufficient for the defects formed in a-SiN$_{1.06}$ to migrate into the a-SiO$_{1.9}$ layer. Furthermore, the elongation rate observed when Au NPs are solely and predominantly surrounded by a-SiO$_{1.9}$ is similar. Thus, the experimental results suggest that the presence of voids has no significant role in the shaping process in a-SiO$_{1.9}$. For a-SiN$_{1.06}$, the presence of voids in all relevant configurations does not allow a direct comparison, thus its influence on the cannot be determined from these experiments.

Based on the presented measurements of the shape transformation of Au NPs embedded in different media the following has been found:

(i) Au NPs do elongate when embedded in a-SiN$_{1.06}$.

(ii) The process is less efficient in a-SiN$_{1.06}$ while the geometry of the elongated Au NPs does not resemble high-aspect-ratio nanorods as in a-SiO$_{1.9}$.

(iii) When the Au NPs are located at the interface of a-SiO$_{1.9}$ and a-SiN$_{1.06}$ they shift towards the a-SiO$_{1.9}$ layer before ion shaping occurs, after which it happens predominantly in the a-SiO$_{1.9}$ layer.

(iv) When Au NPs are embedded in or in contact with the a-SiN$_{1.06}$ layer, the elongated NPs present nanoporosity.

(v) Defective regions are formed in a-SiN$_{1.06}$ with higher fluences, and to a lesser extent in a-SiO$_{1.9}$ when in contact with a-SiN$_{1.06}$, while retaining the directionality along the ion-beam direction. These structures are possibly empty regions or voids.

To better understand the ion-shaping process in the four systems presented, numerical 3D-iTS calculations were carried out. The numerical model provides an estimate of the time evolution of the temperature profile around the NP. The NP/a-SiO$_2$ interface is known to have an influence on the ion shaping process thus, the numerical results will help identify differences in the material response and better understanding of the presented experimental observations.

C. Effect of the thermophysical materials properties on the ion-shaping process

The morphology of ion tracks in a-SiN$_{1.06}$ and a-SiO$_{1.9}$ is very similar; both are composed of an underdense core surrounded by an overdense shell connected by a transition region [36]. The major differences are that a-SiN$_{1.06}$ shows a higher absolute density change (about four times larger) compared to a-SiO$_{1.9}$, yet with smaller total ion track radii, 4.2 ± 0.1 nm in comparison to 5.4 ± 0.1 nm in a-SiO$_{1.9}$ in the case of irradiation with 185 MeV Au [36]. From previous calculations using the one-dimensional version of the i-TS model to explain track formation in a-SiO$_2$ and a-Si$_3$N$_4$, we have observed two fundamental differences in the thermal spike evolution [42]. First, the lower optical band gap of a-Si$_3$N$_4$ leads to a smaller electron-phonon coupling and hence a less efficient energy transfer from the incoming ion to the matrix. Second, the higher thermal conductivity of a-Si$_3$N$_4$ leads to faster cooling and shortens the time where the temperature remains above the melting point by a factor of 1/2 compared to a-SiO$_2$. It can thus be expected that the thermal environment experienced by each Au NP varies significantly depending on the embedding medium. Regarding the impact voids can have on the thermophysical properties of the materials, it is known that the formation of porous media due to the presence of voids has been linked to a decrease in the bulk thermal conductivity of the material [43]. This could potentially lead to an increase in the elongation rate, yet it is accompanied by a decrease in bulk density reducing the energy deposited around the NP and, thus, reducing the efficiency. As the elongation rate observed for Au NPs when embedded solely or predominantly in a-SiO$_{1.9}$ is nearly identical we argue there is little influence of the voids on the efficiency of the process and, thus, the use of bulk values without corrections due to the presence of voids for both materials is supported.

1. Amorphous silicon nitride and silicon dioxide

Figure 9 shows three cross-sectional snapshots of the 3D-iTS calculations at times $t = 0.1$, 1, and 10 ps of the lattice temperature after the passage of an energetic ion through the center of the Au NP while embedded in a-SiO$_{1.9}$ [Fig. 9(a)] and a-SiN$_{1.06}$ [Fig. 9(b)]. At $t = 0.1$ ps, the characteristic thermal profile of the thermal spike governing the ion track formation process can be observed in both dielectric media. Continuous lines have been added to indicate the boundary region for the melting temperature of a-SiO$_2$ (green), a-Si$_3$N$_4$ (blue), and Au (dark yellow). In a-SiO$_2$ [Fig. 9(a)], a region above the melting temperature of Au can be observed around the NP boundary, displaying an early stage of the heating process that moves from the boundary towards the center of the NP. On the two sites of the NP in direct contact with the thermal spike, a molten region of the NP is observed. For a-Si$_3$N$_4$, the lower electron-phonon coupling strength leads to a lower-temperature environment surrounding the Au NP; thus, at this stage, the NP remains completely solid.

At $t = 1$ ps, where both dielectric media are at the early stage of the cooling process, heating and melting of the NP is apparent. In the case of a-SiO$_2$, the Au NP is completely molten and the temperature is almost constant within the NP. Due to the low thermal conductivity of a-SiO$_2$ the formation of an extended region around the NP with a temperature significantly higher than the melting point of a-SiO$_2$ is apparent. This area extends nearly 10 nm beyond the particle boundary in the perpendicular direction to the ion path and nearly 20 nm at the zone in contact with the ion track. This region creates a thermal gradient towards the inner region of the ion track. The thermal profile formed around the Au NP in a-Si$_3$N$_4$ resembles a similar shape to that for a-SiO$_2$, yet the maximum temperatures reached are significantly lower. While the NP is molten, the center remains cooler with respect to the boundary and thus the energy is not homogeneously distributed within the NP volume.
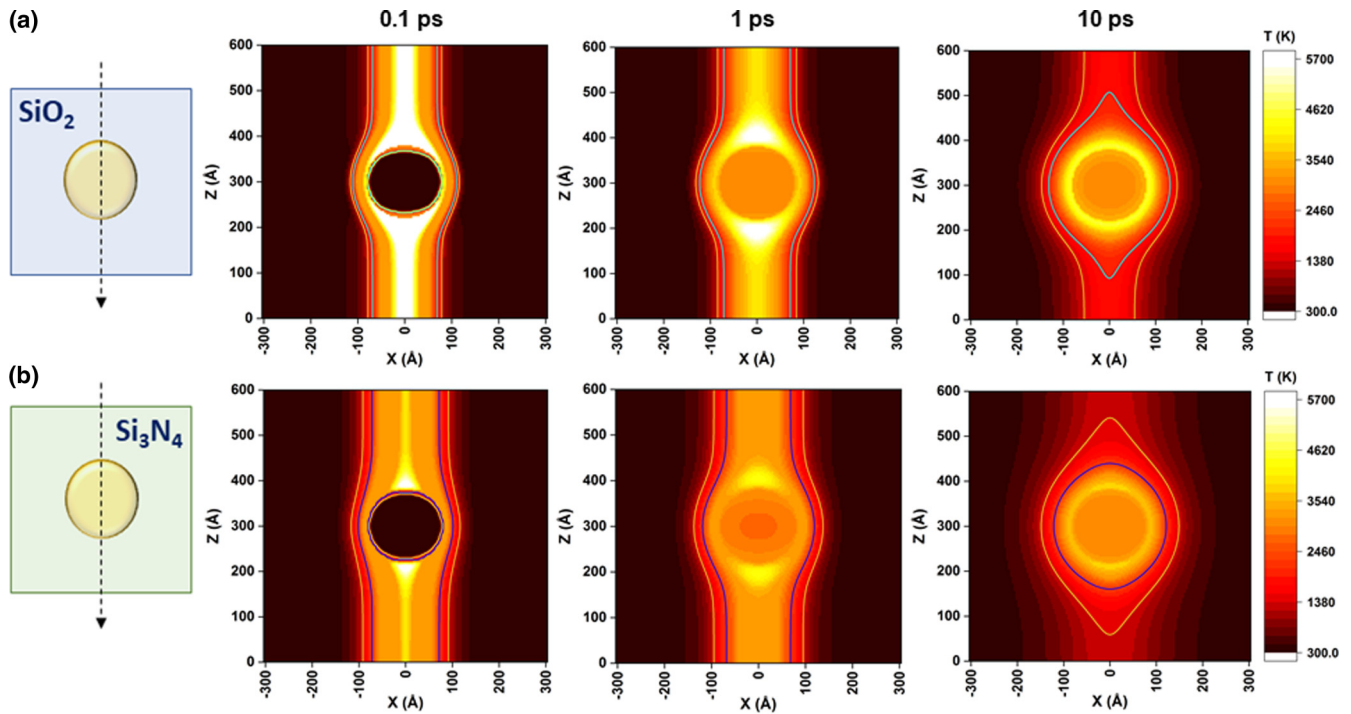
FIG. 9. Configuration of the 3D-TS calculation cell, with snapshots of the three-dimensional thermal evolution of a 16-nm-diameter Au NP while embedded in a-SiO$_2$ (a) and a-Si$_3$N$_4$ (b). Solid lines were added to show the region surpassing the melting point of a-SiN$_{1.06}$ (dark blue), a-SiO$_{1.9}$ (light blue), and Au (dark yellow).

At $t = 10$ ps, the thermal spike is in the later stages of the cooling period for the two dielectric materials. At this stage, it is observed that the temperature within the ion track region in a-SiO$_2$ has fallen below the mean melting point of a-SiO$_2$ but remains above that of Au. At the boundary of the NP, an anisotropic region remains above the melting point of a-SiO$_2$, exhibiting an "eye" shape. For the other case, in a-Si$_3$N$_4$, the region that corresponds to the ion track has cooled down below the melting point of Au. Similar to a-SiO$_2$, around the NP an anisotropic region with an eye shape is formed where the temperature remains above the melting point of Au. A nearly spherical region closer to the NP boundary (of about 5 nm in thickness) remains above the mean melting point of a-Si$_3$N$_4$.

In previous MD simulations [30,44] it was proposed that the most relevant stage of the ion-shaping mechanism occurs between 5 and 20 ps, when the Au NP expands by a longitudinal flow into the underdense core of the ion track. Leino *et al.* [30] showed that the Au NP melts during the first picoseconds while an ion track is formed within the same timescale. Further MD simulations were carried out in the same study to provide insight into the saturation of the width and its dependence on the ion track in a-SiO$_2$. According to their findings, when the width of the track core is smaller than the diameter of the spherical NPs, or the width of the elongated NP as they form with increasing fluence, the NP expands and diffuses more efficiently along the parallel than the perpendicular direction to the beam due to the high temperatures near the ion trajectory, where the substrate exerts pressure on the cluster preventing the growth, resulting in an increase in the aspect ratio. This behavior continues until the width of the NP approaches the width of the underdense track

core. In this scenario the NP expands in all directions with the same efficiency. In the current paper we intend to identify the level of agreement between the MD simulations and the current experimental results by analyzing in more detail the 3D-iTS numerical calculations.

Figures 10(a) and 10(b) show the longitudinal temperatures, centered at the cell axis, for the Au NP embedded in a-SiO$_2$ and a-Si$_3$N$_4$, respectively, at relevant times based on the 3D-iTS calculations. Dashed lines represent the position of the metal/dielectric boundary while the dotted lines were added for reference with the known melting temperatures of Au, a-SiO$_2$, and a-Si$_3$N$_4$, respectively. While amorphous materials do not have well-defined melting temperatures, we adopted the values using previous i-TS numerical simulations for a-SiO$_2$ [19] and a-Si$_3$N$_4$ [45]. From the plots it can be seen that after 0.3 ps the ion track is formed before the heating and melting of the Au NP in both a-SiO$_2$ and a-Si$_3$N$_4$. Also, an increase in the temperature in the dielectric layer at the metal/dielectric boundary above that of the metallic NP is observed. Such increase is related to what Dufour *et al.* [38] identified as the outer boundary heating scenario, where the energetic electrons generated during the ion passage in the Au NP spread out, radially transferring kinetic energy to the Au atoms before reaching the metal/dielectric boundary. While the energy transfer in Au is inefficient, at the boundary the electrons transfer their kinetic energy more efficiently due to a higher electron-phonon coupling in a-SiO$_2$ and a-Si$_3$N$_4$ with respect to Au, resulting in the increase of the dielectric lattice temperature at the boundary. This leads to increased heating of the NP at the interface due to the high thermal conductivity of Au, as seen in the plots, from the boundary to the center of the NP. This is also evident when the corresponding temperature
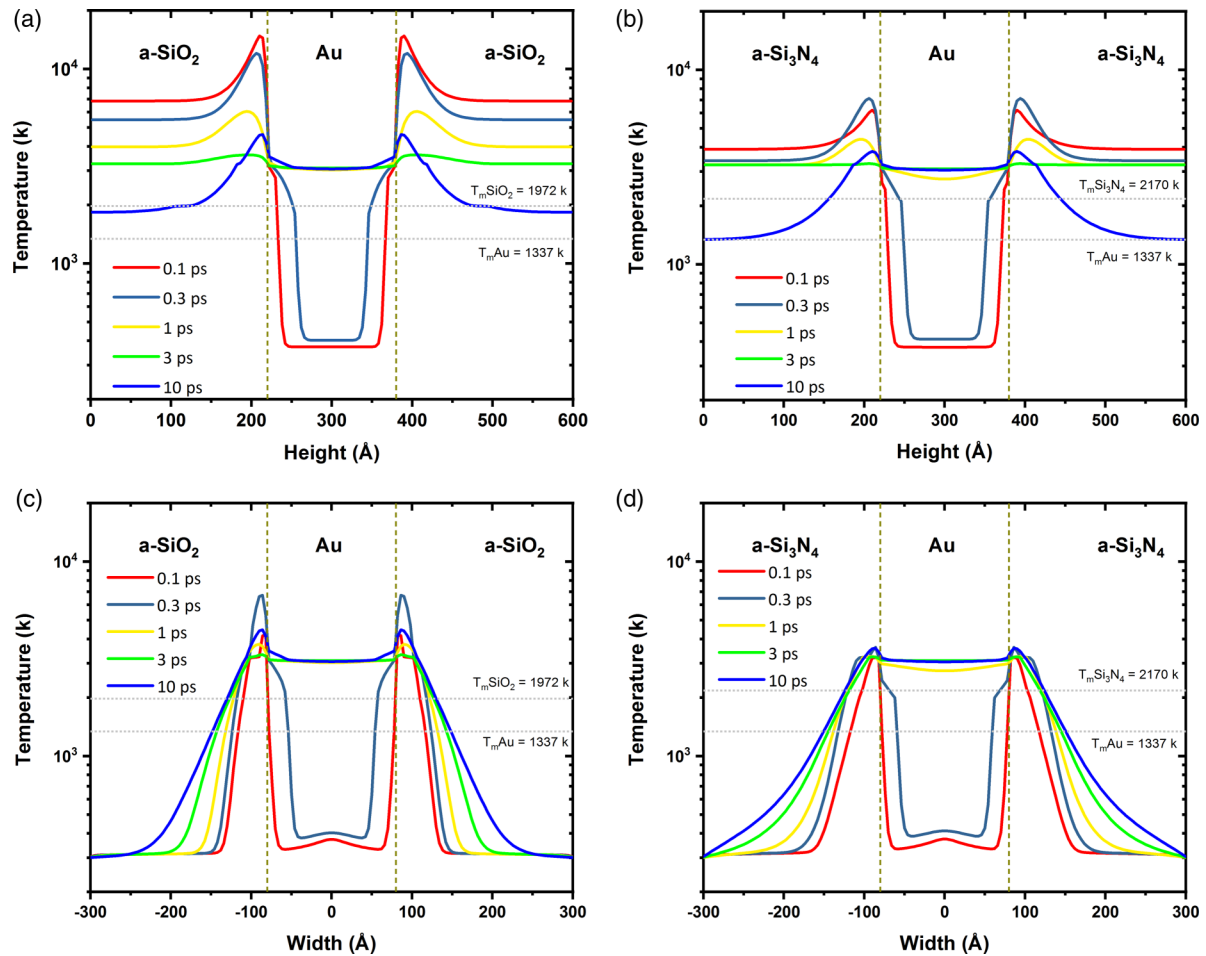
FIG. 10. Longitudinal and transversal temperature profiles through the center of the Au NPs at different times for one Au NP embedded in a-SiO$_2$ (a), (c) and a-Si$_3$N$_4$ (b), (d), respectively. Dashed lines represent the position of the Au/dielectric boundary while dotted lines have been added to outline the melting point of Au and the mean melting point of a-SiO$_2$ and a-Si$_3$N$_4$.

profiles along the direction perpendicular to the beam are plotted for the two systems [Figs. 10(c) and 10(d), for a-SiO$_2$ and a-Si$_3$N$_4$, respectively]. Furthermore, when comparing the parallel and perpendicular temperature profiles with respect to the beam [Figs. 10(a) and 10(c) for a-SiO$_2$ and Figs. 10(b) and 10(d) for a-Si$_3$N$_4$], it is apparent that for both systems the temperature along the parallel direction to the ion beam at the metal/dielectric boundary remains higher than along the direction perpendicular to it, for a duration up to 10 ps.

The temperature profiles calculated using the 3D-iTS model agree with the MD simulations in that the Au NP is molten for longer times than the ion track, longer than 20 ps as suggested by MD simulations [30]. Furthermore, the 3D-iTS calculations show that for a-SiO$_2$ the ion track cools down below the glass transition temperature before 20 ps, closer to 10 ps, and it is the anisotropic region around the boundary that remains above the mean melting point of the corresponding dielectric for longer times. In the eye shaped region of the anisotropic thermal profile surrounding the Au NP, there is a narrow region at the sides of the NP parallel to the beam which remains above the mean melting point of a-SiO$_2$ for longer than 10 ps. As this narrow region matches the location of the underdense track core, the NP might continue expanding for

timescales longer than 10 ps, possibly at lower rates. Thermophoresis thus cannot be ruled out as an additional cause of the anisotropic deformation of the Au NP, as well as a possible flow into the underdense core inferred from the MD simulations.

Furthermore, the saturation width of the deformed NPs is equal or similar to the total track radial dimensions. One would expect that flow into the underdense core would lead to saturation dimensions closer to those of the track core. This has not been addressed by the interpretation of the MD simulations [30]. Therefore, the origin of the elongation of Au NPs might not be solely the result of the flow into the underdense track but a synergetic effect of the outer boundary heating of the NP and the ion track formation process in a-SiO$_2$ near the NP.

Nonetheless, it is observed that in a-SiO$_2$ higher temperatures are reached than in a-Si$_3$N$_4$, a result of the higher electron-phonon coupling in a-SiO$_2$. For a-Si$_3$N$_4$, within the first 10 ps the ion track cools down below the melting point of Au along the parallel direction to the ion beam. This rapid cooling results in transformation of the eye shaped anisotropic region surrounding the NP, which remains above the mean melting point of a-Si$_3$N$_4$, into an almost
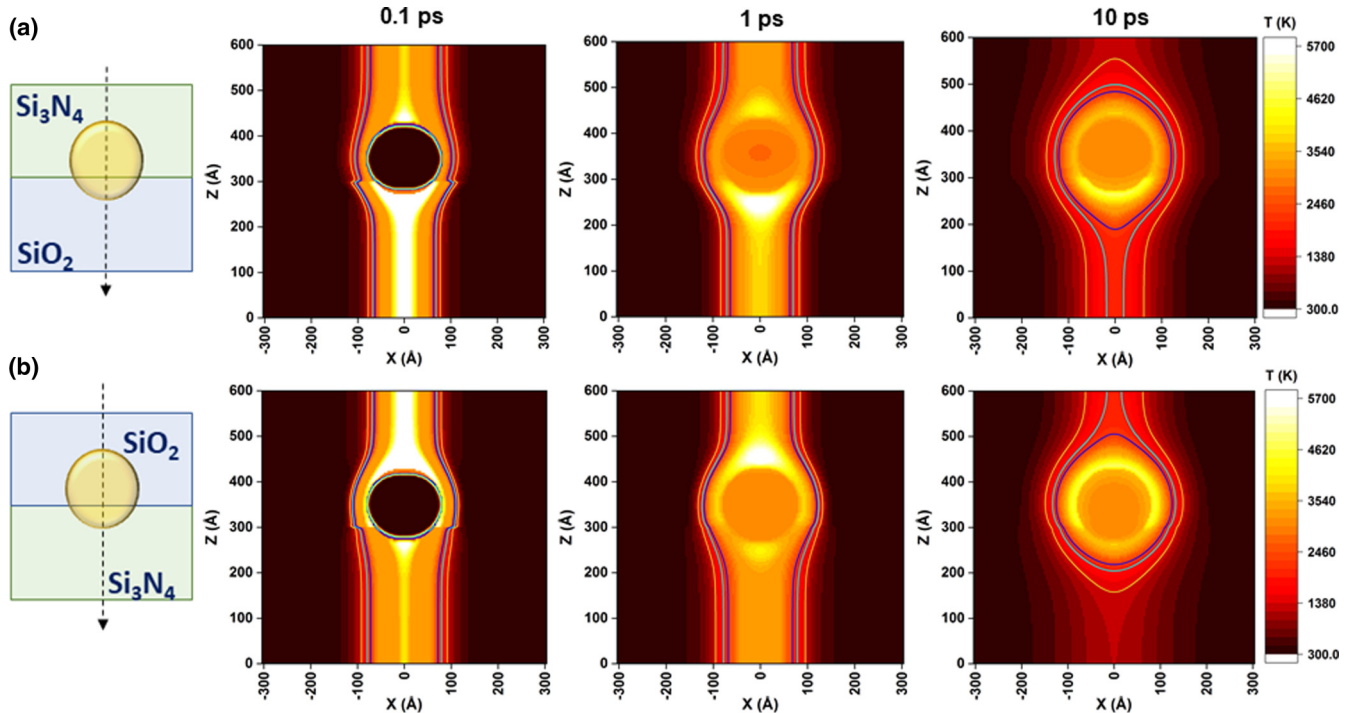
FIG. 11. Cross-sectional schematics and cuts through the three-dimensional calculations of the thermal evolution of a 20-nm-diameter Au NP while embedded in a-Si_3N_4 (top) and a-SiO_2 (bottom) (a) and vice versa (b) based on the i-TS model and considering the passage of an ion through the axis of the NP. Solid lines were added to signal the region corresponding to the melting point of a-$SiN_{1.06}$ (dark blue), a-$SiO_{1.9}$ (light blue), and Au (dark yellow).

isotropic region with a thickness of about 5 nm within the first 10 ps. The reduction in the duration of the anisotropic thermal environment surrounding the Au NP in comparison to a-SiO_2 to almost half might be the reason behind the less efficient shape transformation leading to a rhombiclike geometry with increasing fluence. In the rational description presented by Rizza *et al.* [18], the efficiency of the ion-shaping process was linked to the initial size of the Au NP where the presence of a diamond or faceted geometry is due to a partially molten NP. Thus, the ion-shaping efficiency is dependent not only on the relationship between the ion track radius and the initial NP volume but also on the duration of the formation of the ion track.

2. Competing processes at the amorphous silicon nitride/silicon dioxide interface

The preferential shape transformation towards the a-$SiO_{1.9}$ layer observed when Au NPs are located at the interface of a-$SiO_{1.9}$ and a-$SiN_{1.06}$ layers can also be rationalized in terms of the 3D-iTS model. Figures 11(a) and 11(b) show snapshots of the calculated temperature profile at three representative times (0.1, 1, and 10 ps) for the two configurations studied. There is a similarity in the temperature profiles along the direction parallel to the ion beam of the NP for both configurations and, thus, a similar ion-shaping efficiency is expected for both configurations differentiated only by the material predominantly surrounding the NP.

In the first case, a-Si_3N_4 is the main surrounding medium and it can be observed that from the early stages (0.1 ps) the Au NP experiences two different temperature gradients

along the ion track. The temperature and the thermal gradient are larger at the Au/a-SiO_2 compared to the Au/a-Si_3N_4 boundary. This behavior continues for at least $t = 10$ ps. At this time, the temperature inside the ion track decreases below the melting point of a-Si_3N_4 while on the other end there is still a narrow region above the melting point that extends into the a-SiO_2 layer. For the case where a-SiO_2 is the predominant surrounding medium, along the parallel direction to the beam a very similar behavior is observed as for the first case. As mentioned before, if the migration of Au atoms is governed by the thermal gradient formed at the metal/dielectric boundary, the diffusion is favored towards a-SiO_2 in both cases. The latter is supported by our TEM observations. The corresponding micrographs of samples after irradiation with 3×10^{13} cm^{-2} Au ions do not show an indication of elongation towards a-$SiN_{1.06}$. Instead, the deformation process seems to be characterized by the migration of the Au NP towards the a-$SiO_{1.9}$ layer accompanied by the formation of a slightly curved region at the Au/a-$SiN_{1.06}$ interface. The absence of nanosatellites in a-$SiN_{1.06}$ supports the idea of a low mobility and diffusivity of Au in a-Si_3N_4 for the first case while, for the second, the formation of small NPs around the elongated NP is observed as outlined above for a-$SiO_{1.9}$. As shown in Fig. 6(a) and quantified in Fig. 7(a), the ion-shaping process in this configuration is almost as efficient as when the Au NPs are embedded in a-SiO_2 only.

To better understand the preferential elongation, the temperature profiles parallel to the ion beam are plotted for selected times in Figs. 12(a) and 12(b). At around $t = 0.1$ ps after the passage of the energetic Au ion, an ion track is formed in each layer. Independently, we have characterized
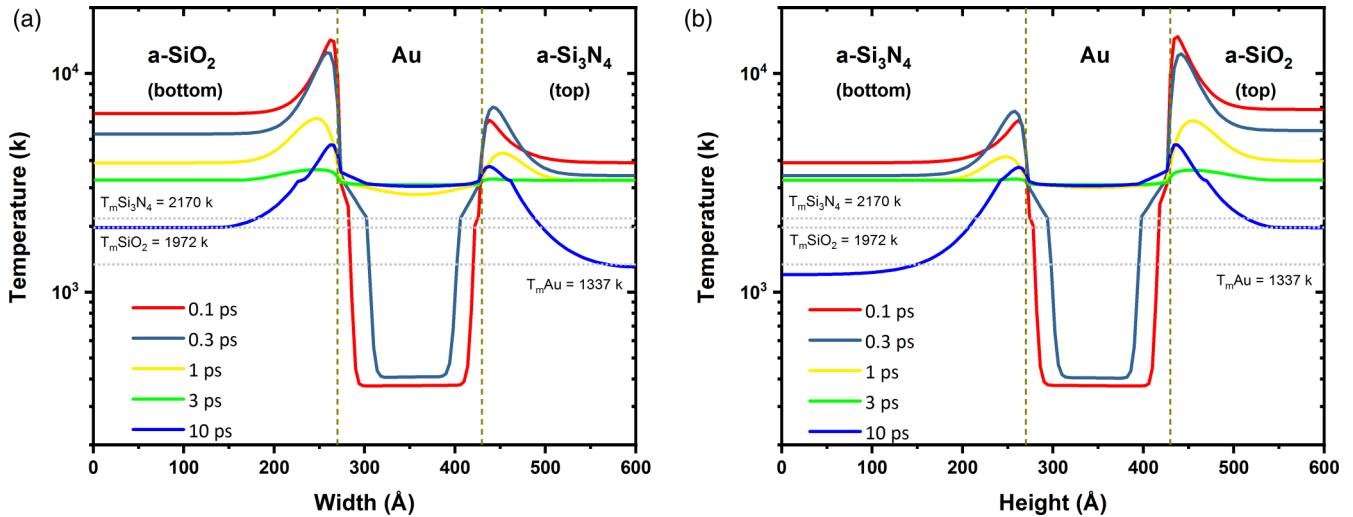
FIG. 12. Longitudinal temperature profile along the Au NP axis for the a-Si$_3$N$_4$/a-SiO$_2$ (top/bottom) (a) and a-SiO$_2$/a-Si$_3$N$_4$ (b) layer configuration. Dashed lines have been added to identify the Au/dielectric boundary position, while the horizontal dotted lines represent the melting point of Au, and the mean melting point of a-SiO$_2$ and a-Si$_3$N$_4$.

the ion track formation in a-SiN$_{1.06}$ and SiO$_{1.9}$ layers by small-angle x-ray scattering, which under similar irradiation energies exhibit an ion track radius of 4.1 ± 0.1 nm for a-SiN$_{1.06}$ and 5.5 ± 0.1 nm for a-SiO$_{1.9}$ with similar morphology, composed of an underdense core surrounded by an overdense shell connected by a smooth transition, where the core dimensions for both materials are very similar [36]. A detailed analysis is available in Refs. [36,37]. As briefly outlined by Leino *et al.* [30], the ion-shaping process of Au NPs is limited by the lifetime of the ion track formation process. In the case of a-SiO$_2$ this occurs within the first 20 ps after the ion passage. For a-Si$_3$N$_4$, however, this process can only occur up to 10 ps [42]. We thus conclude that the difference in the lifetime should significantly influence the ion-shaping process [36].

Using the numerical calculations of the 3D-iTS model we can summarize the following observations:

(i) The ion track is formed before the Au NP increases its temperature in both configurations.

(ii) The temperature reached and the thermal gradient parallel to the beam direction are higher at the Au/a-SiO$_2$ than at the Au/a-Si$_3$N$_4$ interface.

(iii) At $t = 10$ ps in a-Si$_3$N$_4$ the temperature along the ion track direction falls below the melting point while, for a-SiO$_2$, the width of the region along the ion track direction still exhibits a temperature above the melting point narrowed down from about 12 to less than 5 nm.

The observations suggest that in the presence of a NP the formation of the thermal spike is followed by the outer boundary heating process of the NP, a process that takes place between 1 and 100 ps. This process leads to the formation of a local temperature spike at the metal/dielectric boundary where very high temperatures can be reached. This may explain the low-energy threshold observed for ion shaping of ≈ 4 keV/nm in a-SiO$_2$ [46]. As a consequence, the ion-shaping process can take place if the anisotropic thermal profile around the metal/dielectric boundary surpasses the melting temperature

of the surrounding medium, and the efficiency is linked to the duration of this process, which is affected by the thermal conductivity of the surrounding medium.

D. Silicon nitride as diffusion barrier

When Au NPs located at the interface of a-SiO$_{1.9}$ and a-SiN$_{1.06}$ are irradiated with swift heavy-ions they shift towards and preferentially elongate into the a-SiO$_{1.9}$ layer. This property can be used to achieve directional nanostructuring at embedded interfaces. To demonstrate the use of a-SiN$_{1.06}$ as a confining layer to the ion-shaping process, a thin a-SiO$_{1.9}$ layer was embedded between two a-SiN$_{1.06}$ thin layers such that the thickness of the intermediate a-SiO$_{1.9}$ layer is comparable to the expected length of the formed elongated NPs. To estimate the intermediate layer thickness, we followed the trends in the saturation width for the ion shaping observed at the interface of a-SiN$_{1.06}$/a-SiO$_{1.9}$, in particular when a-SiO$_{1.9}$ is the main surrounding medium. In this scenario, the saturation of the width resembled that of Au NPs embedded in a-SiO$_{1.9}$ solely (towards 8.5 ± 1.7 nm) after irradiation with 1×10^{14} cm^{-2}. At that fluence, a mean length of the nanorods of 75.3 ± 21.9 nm was determined considering volume conservation. However, the results showed that Au NPs can elongate further than 100 nm at fluences above 1×10^{14} cm^{-2} likely due to mass redistribution; thus, for the given size the NPs can be expected to reach a length between 100 and 120 nm considering a mean width of 10 nm. After considering these results, it was decided to deposit an intermediate a-SiO$_{1.9}$ layer of 140.2 ± 0.1-nm thickness to account for potential mass redistribution. The thickness of the top and bottom a-SiN$_{1.06}$ layers was set to 160.0 ± 0.2 nm to reduce heating of the deposited Au thin layer while separating the system from the c-Si substrate and the surface.

Figure 13 shows the transformation from nearly spherical Au NPs into high-aspect-ratio nanorods located at the interface of the a-SiN$_{1.06}$/a-SiO$_{1.9}$ layer as expected, while very
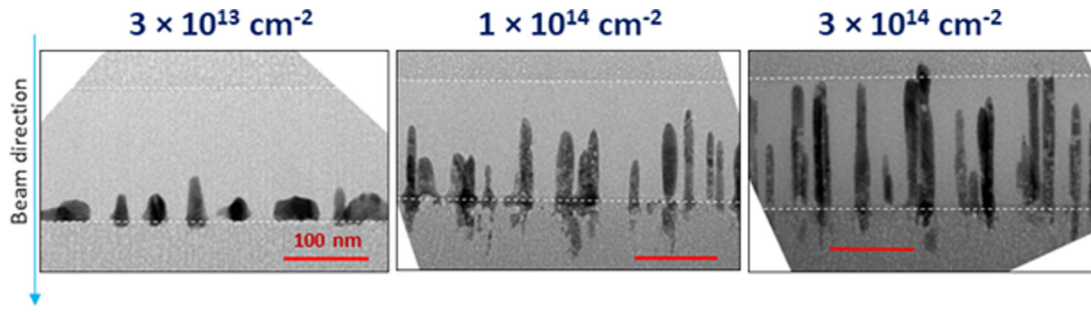
FIG. 13. Cross-section TEM images showing the evolution of the ion-shaping process of Au NPs in a multilayer system with fluence. Dashed white lines were added to outline the location of the a-SiN$_{1.06}$/a-SiO$_{1.9}$ interface.

limited diffusion is observed towards the bottom a-SiN$_{1.06}$ layer. After irradiation with 1×10^{14} cm^{-2}, we observed that the elongated Au NPs exhibit similar width and length values as in the previous sections, with a mean length around 75 nm and without reaching the top layer as expected. When the fluence increases to 3×10^{14} cm^{-2}, the intermediate layer shows that elongated Au NPs reach or are within 5 nm from the top a-SiN$_{1.06}$ layer. Also, for 1×10^{14} and 3×10^{14} cm^{-2}, the formation of small nanorods accompanying the larger elongated NPs is apparent, which can be the result of the variation in the original NP size or due to mass redistribution. Furthermore, the intermediate a-SiO$_{1.9}$ layer develops the formation of defective regions aligned with the beam direction observed at fluences as low as 3×10^{13} cm^{-2}. At these irradiation fluences the Au NPs exhibit nano porosity too, extending through all elongated NPs at the highest fluence.

The NPs that reach, or nearly reach, the top layer show a narrow width distribution with a mean value of 9.1 ± 0.5 nm where no difference in width of the NPs is observed for irradiation with 1×10^{14} and 3×10^{14} cm^{-2}. This suggests that mass redistribution between NPs is involved in the ion-shaping process. If we consider mass conservation, it is possible to approximately calculate the maximum length L_M of a nanorod in terms of its original volume:

$$L_M = \frac{4}{3R_{\text{width}}^2} R_w^2 R_l,$$

where the saturation of the width is represented by R_{width}. As the NP is initially a spheroid, we take into consideration the initial minor R_w and major R_l axes. Considering the initial values as estimated for the Au NP at the a-SiN$_{1.06}$/a-SiO$_{1.9}$ interface, the maximum length possible for a saturation of the width of 9 nm corresponds to $L_M = 65$ nm. The observation of the shorter and longer NPs thus supports the hypothesis that, under the current experimental conditions, Au NPs can elongate beyond the expected length by aggregation of the monomers ejected during the process by neighboring NPs, as previously observed by Kluth *et al.* [47], Dawi *et al.* [48], and Singh *et al.* [49] in the case of Ag NPs. We do not rule out that the observed nanoporosity of the Au NPs facilitates them to elongate further without the necessity of extra material. The mass redistribution, together with the presence of nanoporosity, allows then Au NPs to reach aspect ratios larger than 15:1 at the highest irradiation fluence, yet the top ends of those NPs do not expand into the top layer but are located at the interface of the top layer (within 5 nm from the interface with the upper

a-SiN$_{1.06}$ layer), demonstrating that a-SiN$_{1.06}$ can be used to confine the ion-shaping process to an intermediate a-SiO$_{1.9}$ thin layer.

IV. SUMMARY AND CONCLUSIONS

Experimental observations of the shape transformation of nearly spherical Au NPs about 20 nm in width and 16 nm in length, upon irradiation with 185-MeV Au ions in a-SiO$_{1.9}$, a-SiN$_{1.06}$ and when located at the interface of two dielectric materials, have been presented. When the NPs are embedded in a single layer, a difference in the geometry of the elongated NPs, as well as a higher deformation rate in a-SiO$_{1.9}$ compared to a-SiN$_{1.06}$, are observed. The differences have been discussed in terms of calculations performed using a 3D-iTS model. Clear differences in the thermal profile experienced by the Au NPs due to the specific combination of electron-phonon coupling strength and thermal conductivity in the two host materials are apparent. Furthermore, such differences become more relevant when the NPs are located at the interface of a-SiO$_{1.9}$ and a-SiN$_{1.06}$, where preferential elongation towards the a-SiO$_{1.9}$ layer was observed for all configurations studied. The comparison of the calculated thermal environments for the first four cases studied suggests that the thermal conductivity plays a major role for the local temperature profile at the metal/dielectric boundary, which should have a major influence on the shape transformation process. Furthermore, the elongated Au NPs embedded in, or in contact with, the a-SiN$_{1.06}$ lead to the formation of nanoporous regions, in particular near the a-SiO$_{1.9}$/a-SiN$_{1.06}$ boundary. In addition, defective regions are formed in a-SiN$_{1.06}$ at higher fluences, and to a lesser extent in a-SiO$_{1.9}$ when in contact with a-SiN$_{1.06}$, while retaining the directionality along the ion-beam direction. These are possibly formed by empty regions or voids facilitated by N$_2$ nanobubble formation. Thus, the formation of the defective region in a-SiO$_{1.9}$ and inside the Au NPs could be the result of damage diffusion from the a-SiN$_{1.06}$ layer. Finally, it is demonstrated that a-SiN$_{1.06}$ can be used as a material to confine the ion-shaping process into an intermediate a-SiO$_{1.9}$ layer, where the dimensions of the layer can be varied.

[1] Editorial, Surface plasmon resurrection, Nat. Photonics **6**, 707 (2012).

[2] R. Zia, J. A. Schuller, A. Chandran, and M. L. Brongersma, Plasmonics: The next chip-scale technology, Mat. Today **9**, 20 (2006).

[3] C. Noguez, Surface plasmons on metal nanoparticles: The influence of shape and physical environment, J. Phys. Chem. C **111**, 3806 (2007).

[4] P. Mühlschlegel, H.-J. Eisler, O. J. F. Martin, B. Hecht, and D. W. Pohl, Resonant optical antennas, Science **308**, 1607 (2005).

[5] K. Li, M. I. Stockman, and D. J. Bergman, Self-Similar Chain of Metal Nanospheres as an Efficient Nanolens, Phys. Rev. Lett. **91**, 227402 (2003).

[6] H. Amekura, N. Ishikawa, N. Okubo, M. C. Ridgway, R. Giulian, K. Mitsuishi, Y. Nakayama, C. Buchal, S. Mantl, and N. Kishimoto, Zn nanoparticles irradiated with swift heavy ions at low fluences: Optically-detected shape elongation induced by nonoverlapping ion tracks, Phys. Rev. B **83**, 205401 (2011).

[7] M. Bayle, C. Bonafos, P. Benzo, G. Benassayag, B. Pécassou, L. Khomenkova, F. Gourbilleau, and R. Carles, Ag doped silicon nitride nanocomposites for embedded plasmonics, Appl. Phys. Lett. **107**, 101907 (2015).

[8] J. A. Reyes-Esqueda, C. Torres-Torres, J. C. Cheang-Wong, A. Crespo-Sosa, L. Rodriguez-Fernandez, C. Noguez, and A. Oliver, Large optical birefringence by anisotropic silver nanocomposites, Opt. Express **16**, 710 (2008).

[9] P. E. Mota-Santiago, A. Crespo-Sosa, J. L. Jiménez-Hernández, H. G. Silva-Pereyra, J. A. Reyes-Esqueda, and A. Oliver, Size characterisation of noble-metal nano-crystals formed in sapphire by ion irradition and subsequent thermal annealing, Appl. Surf. Sci. **259**, 574 (2012).

[10] O. Sánchez-Dena, P. Mota-Santiago, L. Tamayo-Rivera, E. V. García-Ramírez, A. Crespo-Sosa, and J. A. Reyes-Esqueda, Size-and shape-dependent nonlinear optical response of au nanoparticles embedded in sapphire, Opt. Mater. Express **4**, 92 (2014).

[11] M. Jahn, S. Patze, I. J. Hidi, R. Knipper, A. J. Radu, A. Muhlig, S. Yuksel, V. Peksa, K. Weber, T. Mayerhofer, D. Cialla-May, and J. Popp, Plasmonic nanostructures for surface enhanced spectroscopic methods, Analyst **141**, 756 (2016).

[12] C. D'Orléans, J. P. Stoquert, C. Estournès, C. Cerruti, J. J. Grob, J. L. Guille, F. Haas, D. Muller, and M. Richard-Plouet, Anisotropy of Co nanoparticles induced by swift heavy ions, Phys. Rev. B **67**, 220101(R) (2003).

[13] W. Wesch and E. Wendler, *Ion Beam Modification of Solids* (Springer, New York, 2016).

[14] S. Roorda, T. van Dillen, A. Polman, C. Graf, A. van Blaaderen, and B. J. Kooi, Aligned gold nanorods in silica made by ion irradiation of core-shell colloidal particles, Adv. Mater. **16**, 235 (2004).

[15] Y. K. Mishra, F. Singh, and D. K. Avasthi, Synthesis of elongated Au nanoparticles in silica matrix by ion irradiation, Appl. Phys. Lett. **91**, 063103 (2007).

[16] P. Kluth, R. Giulian, D. J. Sprouster, C. S. Schnor, A. P. Byrne, D. J. Cookson, and M. C. Ridgway, Energy dependent saturation width of swift heavy ion shaped embedded Au nanoparticles, Appl. Phys. Lett. **94**, 113107 (2009).

[17] E. A. Dawi, A. M. Vredenberg, G. Rizza, and M. Toulemonde, Ion-induced elongation of gold nanoparticles in silica by irradiation with Ag and Cu swift heavy ions: Track radius and energy loss threshold, Nanotechnology **22**, 215607 (2011).

[18] G. Rizza, P. E. Coulon, V. Khomenkov, C. Dufour, I. Monnet, M. Toulemonde, S. Perruchas, T. Gacoin, D. Mailly, X. Lafosse, C. Ulysse, and E. A. Dawi, Rational description of the ion-beam shaping mechanism, Phys. Rev. B **86**, 035450 (2012).

[19] K. Awazu, X. Wang, M. Fujimaki, and J. Tominaga, Elongation of gold nanoparticles in silica glass by irradiation with swift heavy ions, Phys. Rev. B **78**, 054102 (2008).

[20] A. Oliver, J. A. Reyes-Esqueda, J. C. Cheang-Wong, C. E. Roman-Velazques, A. Crespo-Sosa, L. Rodriguez-Fernandez, J. A. Seman, and C. Noguez, Controlled anisotropic deformation of Ag nanoparticles by Si ion irradiation, Phys. Rev. B **74**, 245425 (2006).

[21] O. Pena-Rodriguez, A. Prada, J. Olivares, A. Oliver, L. Rodriguez-Fernandez, H. G. Silva-Pereyra, E. Bringa, J. M. Perlado, and A. Rivera, Understanding the ion-induced elongation of silver nanoparticles embedded in silica, Sci. Rep. **7**, 922 (2017).

[22] H. Kumar, S. Ghosh, D. Avasthi, D. Kabiraj, A. Mucklich, S. Zhou, H. Schmidt, and J. P. Stoquert, Ion beam-induced shaping of Ni nanoparticles embedded in a silica matrix: From spherical to prolate shape, Nanoscale Res. Lett. **6**, 155 (2011).

[23] M. C. Rdigway, R. Giulian, D. J. Sprouster, P. Kluth, L. L. Araujo, D. J. Llewellyn, A. P. Byrne, F. Kremer, P. F. P. Fichtner, G. Rizza, H. Amekura, and M. Toulemonde, Role of Thermodynamics in the Shape Transformation of Embedded Metal Nanoparticles Induced by Swift Heavy-Ion Irradiation, Phys. Rev. Lett. **106**, 095505 (2011).

[24] H. Amekura, N. Okubo, and N. Ishikawa, Optical birefringence of Zn nanoparticles embedded in silica induced by swift heavy-ion irradiation, Opt. Express **22**, 29888 (2014).

[25] H. Amekura, N. Ishikawa, N. Okubo, Y. Nakayama, and K. Mitsuishi, Asynchronous melting of embedded metal nanoparticles and silica matrix for shape elongation induced by swift heavy ion irradiation, Nucl. Instrum. Methods B **269**, 2730 (2011).

[26] H. Amekura, M. L. Sele, N. Ishikawa, and N. Okubo, Thermal stability of embedded metal nanoparticles elongated by swift heavy ion irradiation: Zn nanoparticles in a molten state but preserving elongated shapes, Nanotechnology **23**, 095704 (2012).

[27] G. Rizza, F. Attouchi, P.-E. Coulong, S. Perruchas, T. Gacoin, I. Monnet, and L. Largeau, Rayleigh-like instability in the ion-shaping of Au-Ag allow nanoparticles embedded within a silica matrix, Nanotechnology **22**, 175305 (2011).

[28] M. Shirai, K. Tsumori, M. Kutsuwada, K. Yasuda, and S. Matsumara, Morphological change in FePt nanogranular thin films induced by swift heavy ion irradiation, Nucl. Instrum. Methods B **267**, 1787 (2009).

[29] S. Klaumunzer, Modification of nanostructures by high-energetic ion beams, Nucl. Instrum. Methods Phys. Res. B **244**, 1 (2006).

[30] A. A. Leino, O. H. Pakarinen, F. Djurabekova, K. Nordlund, P. Kluth, and M. C. Ridgway, Swift heavy ion shape transformation of Au nanocrystals mediated by molten material flow and recrystallization, Mater. Res. Lett. **2**, 37 (2014).

[31] H. Amekura, Shape elongation of embedded metal nanoparticles induced by irradiation with swift heavy ions/cluster ions, in *Proceedings of the Nanotechnology Materials and Devices Conference (NMDC), Toulouse* (IEEE, 2016), pp. 1–2.

[32] N. Itoh, D. M. Duffy, S. Khakshouri, and A. M. Stoneham, Making tracks: Electronic excitation roles in forming swift heavy ion tracks, J. Phys.: Condens. Matter **21**, 474205 (2009).

[33] M. R. Waligorski, R. N. Hamm, and R. Katz, The radial distribution of dose around the path of a heavy ion in liquid water, Nucl. Tracks Radiat. Meas. **11**, 309 (1986).

[34] G. Schiwietz, K. Czerki, M. Roth, F. Staufenbiel, and P. L. Grande, Femtosecond dynamics: Snapshots of the early ion-track evolution, Nucl. Instrum. Methods B **225**, 4 (2004).

[35] F. F. Komarov, Defect and track formation in solids irradiated by superhigh-energy ions, Phys. Usp. **46**, 1253 (2003).

[36] P. Mota-Santiago, T. Bierschenk, F. Kremer, A. Nadzri, H. Vazquez, F. Djurabekova, K. Nordlund, C. Trautmann, S. Mudie, M. C. Ridgway, and P. Kluth, Nanoscale density fluctuations induced by energetic heavy ions in silicon nitride and silicon dioxide, Nanotechnology **29**, 144004 (2018).

[37] P. Kluth, C. S. Schnohr, O. H. Pakarinen, F. Djurabekova, D. J. Sprouster, R. Giulian, M. C. Ridgway, A. P. Byrne, C. Trautmann, D. J. Cookson, K. Nordlund, and M. Toulemonde, Fine Structure in Swift Heavy Ion Tracks in Amorphous SiO$_2$, Phys. Rev. Lett. **101**, 175503 (2008).

[38] C. Dufour, V. Khomenkov, G. Rizza, and M. Toulemonde, Ion-matter interaction: The three-dimensional version of the thermal spike model. Application to nanoparticle irradiation with swift heavy ions, J. Phys. D **45**, 065302 (2012).

[39] T. H. Y. Vu, C. Dufour, V. Khomenkov, A. A. Leino, F. Djurabekova, K. Nordlund, P.-E. Coulon, G. Rizza, and M. Hayoun, Elongation mechanism of the ion shaping of embedded gold nanoparticles under swift heavy ion irradiation, Nucl. Instrum. Methods B **451**, 42 (2019).

[40] B. Schmidt, A. Mucklich, L. Rontzsch, and K.-H. Heining, How do high energy heavy-ions shape Ge nanoparticles embedded in SiO$_2$, Nucl. Instrum. Methods B **257**, 302007.

[41] J. F. Ziegler, M. D. Ziegler, and J. P. Biersack, SRIM: The stopping and range of ions in matter (2010), Nucl. Instrum. Methods B **268**, 1818 (2010).

[42] P. Mota-Santiago, F. Kremer, A. Nadzri, M. C. Ridgway, and P. Kluth, Elongation of metallic nanoparticles at the interface of silicon dioxide and silicon nitride, Nucl. Instrum. Methods B **409**, 328 (2017).

[43] D. S. Smith, A. Alzina, J. Bourret, B. Nait-Ali, F. Pennec, N. Tessier-Doyen, K. Otsu, H. Matsubara, P. Elser, and U. T. Gonzenbach, Thermal conductivity of porous materials, J. Mater. Res. **28**, 2260 (2013).

[44] A. Leino, O. Pakarinen, F. Djurabekova, and K. Nordlund, A study on the elongation of embedded Au nanoclusters in SiO$_2$ by swift heavy ion irradiation using MD simulations, Nucl. Instrum. Methods B **282**, 76 (2012).

[45] T. Kitayama, Y. Morita, K. Nakajima, K. Narumi, Y. Saitoh, M. Matsuda, M. Sataka, M. Tsujimoto, S. Isoda, M. Toulemonde, and K. Kimura, Formation of ion tracks in amorphous silicon nitride films with MeV C60, Nucl. Instrum. Methods Phys. Res. B, **356-357**, 22 (2015).

[46] H. Amekura, P. Kluth, P. Mota-Santiago, I. Sahlnerg, V. Jantunen, A. A. Leino, H. Vazquez, K. Nordlund, F. Djurabekova, N. Okubo, and N. Ishikawa, Vapor-like phase of amorphous SiO$_2$ is not a prerequisite for the core-shell ion tracks or ion shaping, Phys. Rev. Materials **2**, 096001 (2018).

[47] P. Kluth, B. Johannessen, R. Giulian, C. S. Schnohr, G. J. Foran, D. J. Cookson, A. P. Byrne, and M. C. Ridgway, Ion irradiation effects on metallic nanocrystals, Rad. Eff. & Def. in Sol. **162**, 501 (2007).

[48] E. A. Dawi, G. Rizza, M. P. Mink, A. M. Vredenberg, and F. H. P. M. Habraken, Ion beam shaping of Au nanoparticles in silica: Particle size and concentration dependence, J. Appl. Phys. **105**, 074305 (2009).

[49] F. Singh, S. Mohapatra, J. P. Stoquert, D. K. Avasthi, and J. C. Pivin, Shape deformation of embedded metal nanoparticles by swift heavy ion irradiation, Nucl. Instrum. Methods B **267**, 936 (2009).